J|A|C|S
JOURNAL OF THE AMERICAN CHEMICAL SOCIETY
Article
pubs.acs.org/JACS

Probing the Lower Limit of Lattice Thermal Conductivity in an Ordered Extended Solid: $Gd_{117}Co_{56}Sn_{112}$, a Phonon Glass−Electron Crystal System

Devin C. Schmitt,[†] Neel Haldolaarachchige,[‡] Yimin Xiong,[‡] David P. Young,[‡] Rongying Jin,[‡] and Julia Y. Chan*,[†]

[†]Department of Chemistry, Louisiana State University, Baton Rouge, Louisiana 70803, United States
[‡]Department of Physics and Astronomy, Louisiana State University, Baton Rouge, Louisiana 70803, United States

Ⓢ *Supporting Information*

ABSTRACT: The discovery of novel materials with low thermal conductivity is paramount to improving the efficiency of thermoelectric devices. As lattice thermal conductivity is inversely linked to unit cell complexity, we set out to synthesize a highly complex crystalline material with glasslike thermal conductivity. Here we present the structure, transport properties, heat capacity, and magnetization of single-crystal $Gd_{117}Co_{56}Sn_{112}$, a complex material with a primitive unit cell volume of ~6858 Å^3 and ~285 atoms per primitive unit cell (1140 atoms per face-centered cubic unit cell). The room temperature lattice thermal conductivity of this material is $\kappa_L = 0.28$ W/(m·K) and represents one of the lowest ever reported for a nonglassy or nonionically conducting bulk solid. Furthermore, this material exhibits low resistivity at room temperature, and thus represents a true physical system that approaches the ideal phonon glass−electron crystal.

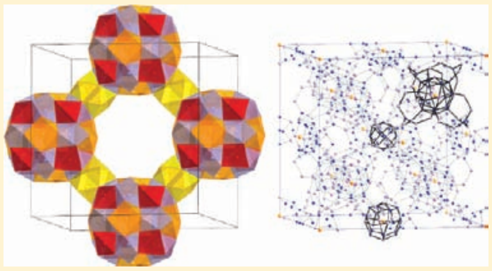

■ INTRODUCTION

One of the most fundamental properties of a solid is its thermal conductivity—a measure of a material's ability to transfer heat. The discovery of novel materials with low thermal conductivity is paramount to improving the efficiency of thermoelectric devices.[1−3] The structural complexity of a material is fundamentally linked to its lattice thermal conductivity, a correlation that is well documented both theoretically[4] and experimentally.[5] Thus, exploring materials with high structural complexity provides an avenue for discovering materials with intrinsically low thermal conductivity. Here we present the structure, transport, and magnetic properties of single-crystal $Gd_{117}Co_{56}Sn_{112}$, a complex material with a primitive unit cell volume of ~6858 Å^3 and ~285 atoms per primitive unit cell (1140 atoms per face-centered cubic unit cell). Since $Gd_{117}Co_{56}Sn_{112}$ is one of the most structurally complex extended solids known, we use the material to probe the limit of lattice thermal conductivity in a nonglassy material with the expectation of glasslike thermal conductivity. Indeed, the room temperature lattice thermal conductivity of this material represents one of the lowest ever reported for a bulk solid. Furthermore, single-crystal $Gd_{117}Co_{56}Sn_{112}$ exhibits low electrical resistivity at room temperature. The concomitant low electrical resistivity and exceptionally low lattice thermal conductivity represents a true physical system that approaches the ideal phonon glass−electron crystal.

The total thermal conductivity of a material, κ_T, can be separated into a lattice contribution, κ_L, and an electronic contribution, κ_e, where $\kappa_T = \kappa_L + \kappa_e$. κ_e is often less than 1 W/(m·K) in good thermoelectric materials (semiconductors) due to relatively low optimal carrier concentrations.[1] κ_L is considered a parasitic parameter in a thermoelectric material, where the dimensionless figure of merit, $ZT = S^2T/[\rho(\kappa_e + \kappa_L)]$, is to be maximized. Here, S is the Seebeck coefficient (μV/K), ρ is the electrical resistivity (Ω·cm), and T is the temperature.[1] Furthermore, since the figure of merit is inversely proportional to both ρ and κ, the ideal candidate for a thermoelectric material must exhibit low thermal transfer properties like a glass and simultaneously the electronic properties of a crystalline solid at its operating temperature. A material exhibiting this unusual set of properties was termed a "phonon glass−electron crystal" (PGEC) by Slack.[6] A relationship between κ_e and ρ is given by the Wiedemann−Franz Law, $\kappa_e = L_oT/\rho$, where $L_o = 2.45 \times 10^{-8}$ W·Ω/K^2 is the Lorentz number. Substituting this into the figure of merit leads to $ZT = S^2/[L_o(1 + \kappa_L/\kappa_e)]$. Notably, as κ_L/κ_e approaches zero, the Seebeck coefficient becomes the only contributing factor in determining ZT.

Although amorphous and glassy materials often have very low thermal conductivities, their electrical resistivities are too large to be useful for thermoelectric applications; thus, the focus here is to discover *ordered* crystalline structures that have very low *intrinsic* lattice thermal conductivity. In crystalline systems, such as Zn_4Sb_3,[7] TAGS $[(GeTe)_x(AgSbTe_2)_{100-x}]$,[8] and the LAST $(AgPb_mSbTe_{2+m})$[9] compounds, their thermal

Received: January 9, 2012
Published: February 29, 2012

transport is highly dependent on varying degrees of disorder.[3] The aforementioned materials exhibit glasslike thermal conductivity stemming from partially amorphous structures (Zn_4Sb_3) or substitutional disorder. While these systems often possess a large Seebeck coefficient, they are likely close to the upper limit of their figure of merit values. The challenge with this "extrinsically complex" model is that the lattice imperfections that effectively scatter thermally conducting phonons also scatter charge carriers. Thus, charge carriers in these systems have relatively low mobilities, resulting in an overall high magnitude of the electrical resistivity relative to semiconductors with similar carrier concentrations. Doping to higher carrier concentrations (n) would, of course, decrease electrical resistivity, but the carrier mobility also suffers further from increased carrier−carrier scattering. The thermopower would also likely decline, as the ambipolar Seebeck coefficient term is inversely proportional to n.[1]

There are three ways to intrinsically reduce the thermal conductivity of a lattice: (1) increase lattice complexity, (2) introduce a nonhomogeneous harmonic oscillator (a "rattler" atom), and (3) use atoms with a high average atomic mass such as Sn, Te, Yb, Bi, etc. Here we focus on (1) and (3). A complex many-atom unit cell can scatter phonons that carry heat efficiently by a factor of $1/N$, where N is the number of atoms in the primitive unit cell, effectively lowering κ_L.[5,10] With its complex structure containing 285 atoms in the primitive cell, and high atomic mass elements, $Gd_{117}Co_{56}Sn_{112}$ is a promising candidate as an intrinsically low lattice thermal conductivity material.

EXPERIMENTAL SECTION

Synthesis. Starting materials for the preparation of $Gd_{117}Co_{56}Sn_{112}$ were ingots of Gd, Co powder, and Sn shot (all >99.9 wt % purity, metal basis) and were used as received. Gd, Co, and Sn were loaded (in desired molar ratios discussed below) into an alumina crucible and sealed in an evacuated ($\sim 1.2 \times 10^{-3}$ atm) fused silica tube. In growth attempts that exceeded 1200 °C, the tube was filled with ~0.2 atm of Ar to prevent silica tube collapse. The initial synthesis employed heating a molar ratio of 2:1:2 (Gd:Co:Sn) to 1200 °C for 8 h, slow cooling to 1075 at 4 °C/h, followed by fast cooling at 150 °C/h, which led to a minority formation of $Gd_{117}Co_{56}Sn_{112}$, with majority formation of $GdCoSn_2$ with the $CeNiSi_2$ structure type.[11] The use of silica wool in attempts to spin the sample resulted in silicon incorporation in the sample, and the exclusive formation of the $GdCo(Sn,Si)_2$ with the $CeNiSi_2$ structure type.[11] The highest yield of phase pure $Gd_{117}Co_{56}Sn_{112}$ was achieved by heating a molar ratio of 12:6:11 (Gd:Co:Sn) to 1260 °C, slow cooling at 1 °C/h to 1200 °C, followed by faster cooling at 5 °C/h to 1065 °C. The sample was then removed from the oven and allowed to cool to room temperature. Attempts to flux grow $Gd_{117}Co_{56}Sn_{112}$ using a higher Sn:Gd ratio resulted in the exclusive formation of $GdCoSn_2$. This is similar to the appearance of $GdCoSn_2$ when increasing the Sn content (above 44:16:40 of Gd:Co:Sn) in the Gd−Co−Sn ternary phase diagram.[12] $Gd_{117}Co_{56}Sn_{112}$ yields increased significantly as both the maximum dwell temperature and the length of time spent above 1200 °C were increased. $Gd_{117}Co_{56}Sn_{112}$ is highly reactive to both HCl and HNO_3; thus, mechanical extraction was necessary to separate the three different flux free crystal morphologies listed below. The $Gd_{117}Co_{56}Sn_{112}$ phase has a markedly different color, very dark gray polyhedrals, as opposed to $GdCoSn_2$, which forms silvery platelike crystals.[11] A third phase, polycrystalline CoAl, was identified through powder X-ray diffraction and formed a thin layer between the sample and alumina crucible. Our experiments show that high temperatures and approximate equimolar Gd:Sn ratios are required to form the $Gd_{117}Co_{56}Sn_{112}$ phase as opposed to the $GdCoSn_2$ phase.

Elemental Analysis. Elemental analysis was performed by two techniques: (1) energy-dispersive spectroscopy (EDS) using a standard-free JEOL JSM-5060 scanning electron microscope (SEM) with an accelerating voltage of 15 keV and a crystal-to-detector distance of 20 mm and (2) inductive plasma coupled optical emission spectroscopy (ICP-OES), using a Perkin-Elmer Optima 5300 DV with elemental Gd, Co, and Sn as internal standards. By use of an average of 12 scans at different locations on the crystal, the stoichiometry of the sample as determined by EDS was $Gd_{117(10)}Co_{45(10)}Sn_{107(10)}$, and the ICP-OES-determined stoichiometry was $Gd_{117(3)}Co_{48(3)}Sn_{111(3)}$. Error bars were determined by summing a fixed 3 atom % instrumental error and the standard deviations of the data collected for the EDS stoichiometry and using a fixed 1 atom % for the ICP-OES stoichiometry.

X-ray Diffraction. Powder X-ray diffraction was performed to determine phase homogeneity and purity using a Bruker D8 Advance X-ray diffractometer with monochromatic Cu $K\alpha_1$ radiation with λ = 1.540 562 Å ($2\theta_{max}$ = 80°). A single-crystal fragment of $Gd_{117}Co_{56}Sn_{112}$ was cleaved to approximate dimensions of $0.03 \times 0.08 \times 0.08$ mm^3 and mounted on a glass fiber using epoxy. Single-crystal X-ray diffraction was performed using a Nonius Kappa CCD X-ray diffractometer equipped with a graphite monochromator and Mo $K\alpha$ radiation (λ = 0.710 73 Å). Diffraction data were collected at room temperature up to θ = 30.0°. Absorption corrections were carried out using multiscan methods based on highly redundant data.[13] Crystallographic parameters are provided in Table 1. Direct methods were used to solve the crystal structure using SIR2002,[14] and refinement was conducted in SHELXL97.[15] Intensity statistics suggested that the space group was centrosymmetric. Systematic absences indicated space groups $Fm\bar{3}m$ and $Fm\bar{3}$, and the final model solution was obtained in $Fm\bar{3}m$. The refined stoichiometry of the crystallographic model is $Gd_{117}Co_{56.3(1)}Sn_{111.5(1)}$, but for simplicity we refer to the stoichiometry as $Gd_{117}Co_{56}Sn_{112}$. Atomic parameters for $Gd_{117}Co_{56}Sn_{112}$ can be found in Table 2.

Table 1. Crystallographic Parameters for $Gd_{117}Co_{56}Sn_{112}$

formula	$Gd_{117}Co_{56.3(1)}Sn_{111.5(1)}$
crystal system	cubic
space group	$Fm\bar{3}m$
a (Å)	30.159(3)
V (Å^3)	27432(5)
Z	4
crystal dimensions (mm^3)	$0.03 \times 0.05 \times 0.05$
temperature (K)	298(2)
θ range (deg)	3.51−29.99
μ (mm^{-1})	41.036
data collection	
measured reflections	96152
unique reflections	2013
reflections with $I > 2\sigma(I)$	1637
R_{int}	0.0495
h	−42 to 42
k	−29 to 30
l	−28 to 28
refinement	
$\Delta\rho_{max}$ (eÅ^{-3})/$\Delta\rho_{min}$ (eÅ^{-3})	3.778/−3.371
GoF	1.492
extinction coefficient	0.0000006(1)
reflections/parameters	2013/101
$R_1(F^2 > 2\sigma F^2)^a$	0.0318
$wR_2(F^2)^b$	0.0548

$^aR_1\ \sum[|F_o| - |F_c|]/\sum|F_o|$. $^bwR_2 = [\sum[w(F - F_c^2)]/\sum[w(F_o^2)^2]]^{1/2}$.

Physical Properties. Physical properties were measured on a large single-crystal fragment polished to a bar with dimensions of 1.22 ×

Table 2. Atomic Positions of $Gd_{117}Co_{56}Sn_{112}$

atom	site	x	y	z	occ	U_{eq} (Å^2)^a
Gd1	96*k*	0.067788(14)	0.067788(14)	0.15507(2)	1	0.00966(13)
Gd2	96*k*	0.179230(14)	0.179230(14)	0.40586(2)	1	0.00952(13)
Gd3	96*k*	0.200403(13)	0.200403(13)	0.067189(19)	1	0.00763(13)
Gd4	96*j*	0.253620(19)	0.105016(19)	0	1	0.00806(13)
Gd5	48*i*	0.11773(18)	0.11773(18)	1/2	0.59(3)	0.0080(3)
Gd5′	48*i*	0.1243(2)	0.1243(2)	1/2	0.41(3)	0.0080(3)
Gd6	24*e*	0.3486(2)	0	0	0.555(14)	0.0093(4)
Gd6’	24*e*	0.3356(3)	0	0	0.445(14)	0.0093(4)
Gd7	8*c*	1/4	1/4	1/4	1	0.0085(4)
Gd8	4*a*	0	0	0	1	0.0113(6)
Co1	96*k*	0.16926(4)	0.16926(4)	0.23133(5)	1	0.0099(3)
Co2	96*k*	0.07970(7)	0.07970(7)	0.01525(10)	0.5	0.0107(7)
Co3	32*f*	0.39274(7)	0.39274(7)	0.39274(7)	1	0.0213(7)
Co4	32*f*	0.30774(5)	0.30774(5)	0.30774(5)	1	0.0055(5)
Co5	24*e*	0.4845(9)	0	0	0.088(7)	0.01^b
Co6	32*f*	0.05714(12)	0.05714(12)	0.05714(12)	0.417(12)	0.005(2)
Co7	24*e*	0.4223(14)	0	0	0.076(8)	0.01^b
Sn1	96*k*	0.072852(19)	0.072852(19)	0.32321(3)	1	0.00783(17)
Sn2	96*k*	0.108378(18)	0.108378(18)	0.24026(3)	1	0.00823(17)
Sn3	48*i*	0.20865(3)	0.20865(3)	1/2	1	0.0101(2)
Sn4	48*h*	0.14535(3)	0.14535(3)	0	1	0.0073(2)
Sn5	48*g*	1/4	1/4	0.14087(4)	1	0.0078(2)
Sn6	32*f*	0.14657(3)	0.14657(3)	0.14657(3)	1	0.0090(3)
Sn7	24*e*	0.10880(6)	0	0	0.917(7)	0.0085(6)
Sn8	24*e*	0.21581(5)	0	0	1	0.0100(3)
Sn9	32*f*	0.4462(3)	0.4462(3)	0.4462(3)	0.89(5)	0.0281(14)
Sn9′	32*f*	0.4374(15)	0.4374(15)	0.4374(15)	0.11(5)	0.0281(14)

$^a U_{eq}$ is defined as $^1/_3$ of the trace of the orthogonalized U_{ij} tensor. ^{b}Atomic displacement parameters fixed for final refinement.

1.05 × 1.98 mm^3. Magnetic measurements were conducted using a Quantum Design Physical Property Measurement System (PPMS). Temperature-dependent electrical resistivity was measured using a standard four-probe dc technique using the PPMS. The thermal conductivity and Seebeck coefficient were measured in the PPMS using the thermal transport option. Heat capacity and Hall resistivity were measured using the PPMS heat capacity option and Van der Pauw method, respectively. The Seebeck coefficient was also independently measured using a comparative technique to a constantan standard on an MMR Technologies sample stage.

■ RESULTS AND DISCUSSION

Structure. $Gd_{117}Co_{56}Sn_{112}$ is isostructural to $Dy_{117}Co_{57}Sn_{112}$[16] and exhibits a very complex crystal structure with 24 atomic positions in the asymmetric unit, positional atomic disorder (Table 2), and 1140 atoms in the face-centered cubic (fcc) unit cell (a = 30.159(3) Å). The crystal structure is similar to the $Tb_{117}Fe_{52}Ge_{112}$ structure type,[17] which is adopted for Ln = Gd and Dy−Tm for the Fe analogues and $Sm_{117}Cr_{52}Ge_{112}$.[18] The $Dy_{117}Co_{57}Sn_{112}$ structure has been reported for Ln = Ce,[19] Pr,[20] Sm,[21] and Gd−Dy,[12,21] as well as a Nd−Ru−Sn analogue.[22] Recently, a full topological structural description was reported for $Sm_{117}Co_{55.6}Sn_{116}$.[21] Our structural model is similar to that of ref 21, which uses a multishell approach for the description of $Sm_{117}Co_{55.6}Sn_{116}$. We have chosen to examine an alternate structural model with the recognition of a Co/Sn bonding framework *and* Sn-centered $Sn@Gd_8/Gd_6$ polyhedra, which are similar to structural motifs found in La_4Ge_3 and $Ca_{31}Sn_{20}$.[23,24] For a more detailed description of modeled disorder, see ref 21.

The crystal structure of $Gd_{117}Co_{56}Sn_{112}$ is composed of several different structural units consisting of bonded Co−Sn, Sn−Sn, and Co−Co units (Figure 1a), as well as Sn-centered polar units (Figure 1b). The structural units are conveniently described with respect to Co5, Gd7, and Gd8 with polar units centered at Sn3, Sn4, Sn6, and Sn8 (Figure 2). The Sn-centered units form $Sn@Gd_8/Gd_6$ polyhedra surrounding and connecting the FCC arrangement of Gd8 centered structural units. Co5- and Gd7-centered structural units occupy the octahedral and tetrahedral sites of the FCC structure, respectively. Figure 1c shows the single-crystal X-ray diffraction pattern for a single crystal of $Gd_{117}Co_{56}Sn_{112}$. The sharpness of the spots in the diffraction pattern indicates long-range order with crystalline periodicity.

Figure 2a shows the Sn3-centered unit, which is coordinated to a bicapped trigonal prism of Gd atoms, $Sn3@Gd_8$, with 4 × Gd3, 2 × Gd2, and 2 × Gd4 atoms at 3.419(1), 3.104(1), and 3.326(1) Å, respectively. Two Sn3-centered units share faces with 4 common Gd3 atoms. The Sn4-centered unit (Figure 2b) is coordinated to a bicapped trigonal prism of Gd atoms, Sn4@Gd8, with 2 × Gd3 atoms, 4 × Gd1 atoms, and 2 × Gd4 at 3.101(1), 3.121(1), and 3.484(1) Å, respectively. The Sn6-centered unit (Figure 2c) is coordinated to a highly distorted trigonal antiprismatic environment axially capped by a $Co1_3$ trigonal unit (vide infra) with 3 × Gd3 atoms at 3.317(1) Å and 3 × Gd1 atoms at 3.370(1) Å. The centroid of the $Co1_3$ trigonal unit lies at only ~2.27 Å from Sn6. The Sn8-centered unit (Figure 2d) is coordinated to 4 × Gd4 atoms at 3.366(1) Å and 4 × Gd8 atoms at 3.423(1) Å in a rectangular antiprismatic arrangement. The Sn3, Sn4, Sn6, and Sn8 coordination environments compare well with the Ge^{4-} isolated anions in the Zintl phase La_4Ge_3, where Ge is coordinated by 8 La atoms, four at 3.057(2) Å and four at 3.437(5) Å.[23]

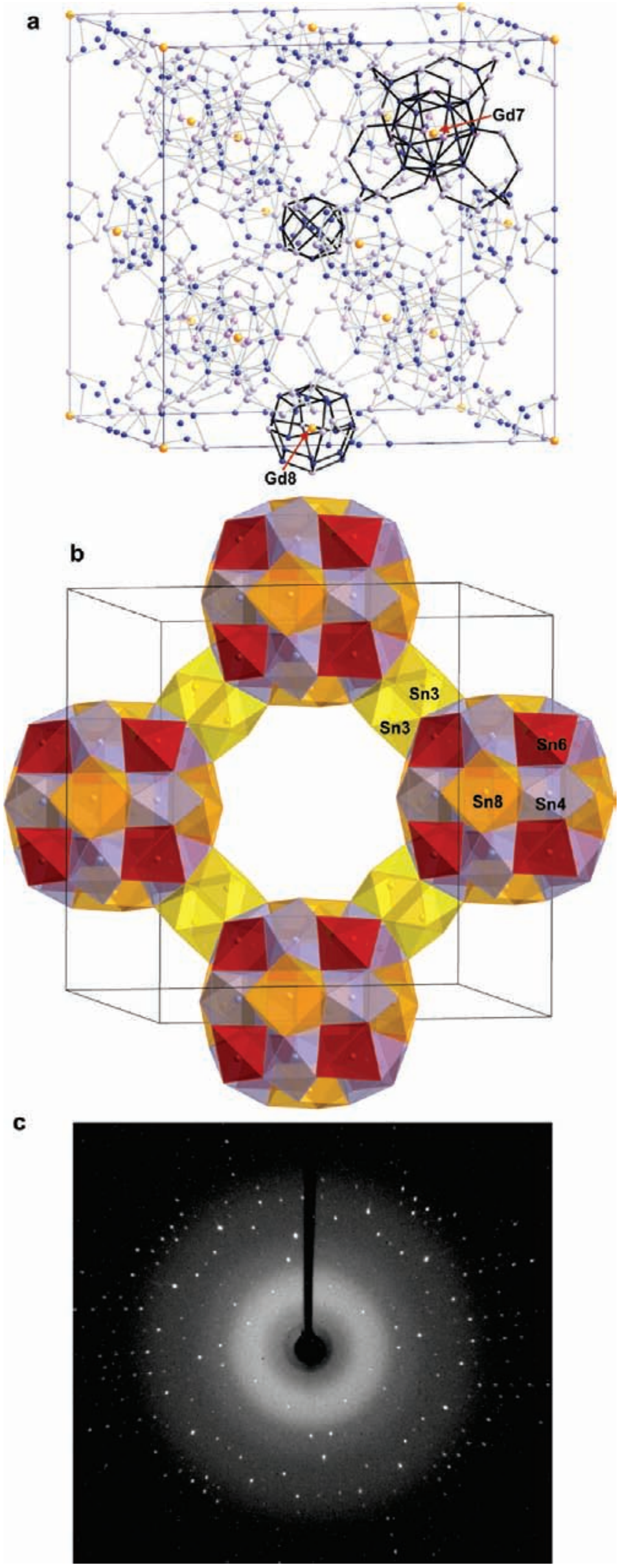

Figure 1. Crystal structure of $Gd_{117}Co_{56}Sn_{112}$. (a) The bonding Co−Sn, Sn−Sn, and Co−Co network within $Gd_{117}Co_{56}Sn_{112}$. Co5- (central unit), Gd7-, and Gd8-centered structural unit bonds are highlighted in black for clarity. (b) Network of Sn3-, Sn4-, Sn6-, and Sn8-centered polyhedra. (c) X-ray diffraction pattern oriented in the 100 direction for a single crystal of $Gd_{117}Co_{56}Sn_{112}$ with a crystal to detector distance of 40 mm and a scan width of 2.0°.

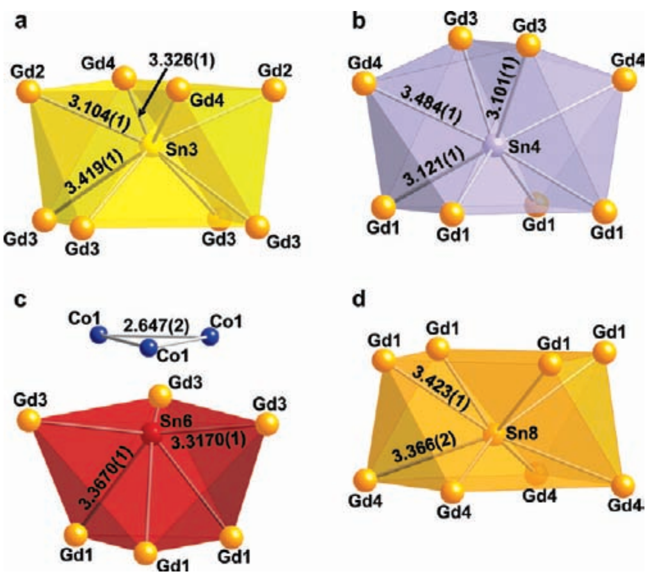

Figure 2. Sn-centered units showing (a) $Sn3@Gd_8$ bicapped trigonal prism, (b) $Sn4@Gd_8$ bicapped trigonal prism, (c) $Sn6@Gd_6Co_3$ axially capped distorted octahedron, and (d) $Sn8@Gd_8$ rectangular antiprism environments.

The Gd7-centered structural unit, as shown in Figure 3a, consists of an inner cage and an outer tetrahedral coordination of peripheral Co−Sn and Sn−Sn bonded atoms. The inner cage is built of an octahedral coordination of Sn5 atoms and a tetrahedral coordination Co4 atoms and $Co1_3$ trigonal units with Co−Co distances of 2.647(2) Å. Each Co4 atom is bonded to three Co1 atoms at 2.505(2) Å, and each Sn5 atom is bonded to four Co1 atoms at 2.642(2) Å. These values are close to the sum of the covalent radii of Co−Co (2.52 Å) and Co−Sn (2.67 Å).[25] The total inner cage coordination is $Gd7@Sn_6Co_{16}$. The inner cages and peripheral atoms are bridged by Co1 and Sn2 atoms with a Co−Sn distance of 2.611(2) Å. The Co−Sn and Sn−Sn network bonded to the peripheral of the inner cage is composed of Sn1, Sn2, and Co3 atoms bonded about the inner cage with tetrahedral symmetry. The arrangement and related bond distances of the atoms are shown in Figure 3a. Each tetrahedral coordination of peripherally linked atoms is made up of three arms extending off a central Co3. The arms consist of an outermost Co3—Sn1 bond (2.560(3) Å), followed by a Sn1—Sn2 bond (2.925(1) Å), and finally a Sn2—Co1 bond (2.611(2) Å) linking the outer atoms to the inner cage. The short Sn1—Sn2 bond distance lies between the anionic-like Sn atoms in $Yb_3Rh_4Sn_{13}$ (2.9672(7) Å) and the strongly bonded zigzag chains of Sn in Yb_3CoSn_6 (2.945(2) Å) and $SrNiSn_2$ (2.843(2) Å).[26−28] The Co−Sn bond distances are similar to those reported (2.50−2.59 Å) for ternary intermetallic compounds, such as $Gd_3Co_4Sn_{13}$, $Ln_4Co_2Sn_5$, and Yb_3CoSn_6.[27,29,30]

The Gd8-centered structural unit, as shown in Figure 3b,c, can be visualized by a unit cell shift of 1/2 along a primary axis. Gd8 is surrounded by an inner cage of Co2, Co6, and Sn7 atoms and a shell of Sn4-, Sn6-, and Sn8-centered units. The inner cage, as shown in Figure 3b, consists of Co2 (50% occupied) and Co6 (41.8(12)% occupied) atoms bonded to Sn7 at 2.600(3) and Co2 at 2.386(4) Å, respectively. The outer shell, as shown in Figure 3c, consists of a cuboctahedral coordination of Sn4 units, a cubic coordination of Sn6 units,

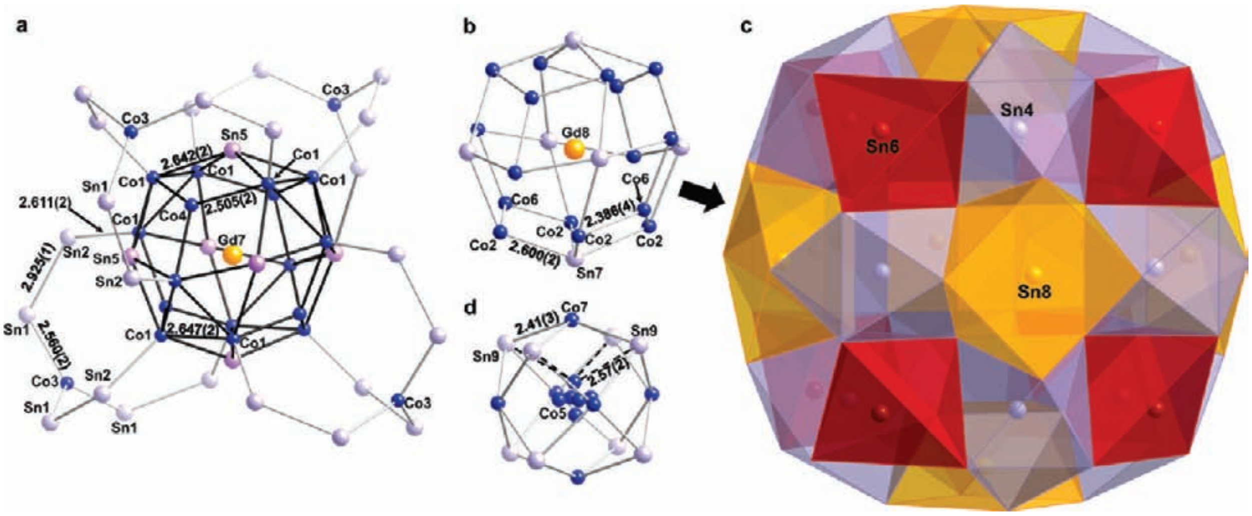

Figure 3. Structural units of Gd$_{117}$Co$_{56}$Sn$_{11}$. (a) Gd7-centered structural unit inner cage (bonds are highlighted in black for clarity) and outer peripheral atoms. (b) Inner cage of the Gd8-centered structural unit with 1/2 of the Co2 (50% occupied) atoms omitted for clarity. (c) Outer coordination of Sn4-, Sn6-, and Sn8-centered units about Gd8. (d) Co6-centered structural unit. The Sn9′ split position is shown as a single position for clarity.

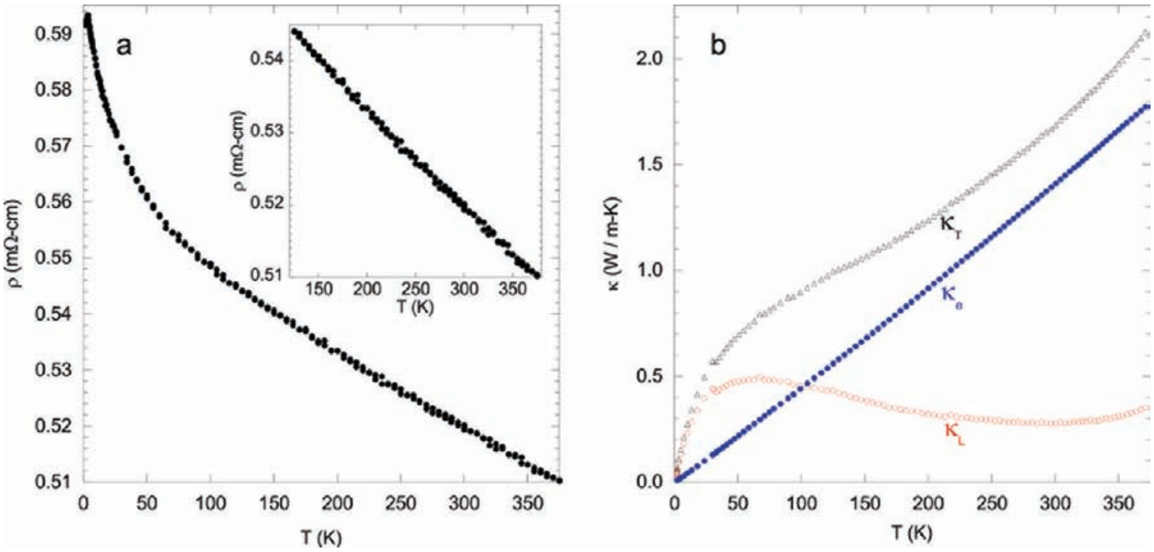

Figure 4. (a) Resistivity as a function of temperature for Gd$_{117}$Co$_{56}$Sn$_{112}$ from 2 to 375 K. The upper inset shows the linearly decreasing resistivity over the temperature range 125−375 K. (b) Thermal conductivity as a function of temperature for Gd$_{117}$Co$_{56}$Sn$_{112}$ from 2 to 375 K. κ_T is the total thermal conductivity, and κ_e and κ_L are the electronic and lattice thermal conductivities, respectively.

and a tetrahedral coordination of Sn8 units. Although Gd8-centered structural units pack in a fcc arrangement, only the four face-centered Gd8 structural units along the (2 0 0) plane are shown in Figure 1b for clarity (a video of the 10 remaining Gd8 structural units centered on the cubic vertices and two remaining face centers is provided in Supporting Information). Gd8-centered structural units are connected by face sharing Sn3 units shown in Figure 1b and Figure 2a.

The Co5-centered structural unit, as shown in Figure 3d, consists of a cubic orientation of Sn9 atoms capped on each face by partially occupied Co7 atoms, Co5@Sn$_8$Co$_6$. The Sn9—Sn9 distance (3.245(13) Å) is comparable to Gd$_3$Co$_4$Sn$_{13}$ and SrSn$_4$ (3.219 and 3.287 Å, respectively), which are considered weakly bonded or nonbonding.[31,32] The Sn9 cubic cage is bonded together by partially occupied Co7 at a distance of 2.40(3) Å, which is shorter than typical Co−Sn bond distances of 2.50−2.59 Å for ternary intermetallic compounds, such as Gd$_3$Co$_4$Sn$_{13}$, Ln$_4$Co$_2$Sn$_5$, and Yb$_3$CoSn$_6$.[27,29,30] Splitting of the Sn9 position allows the Co−Sn bond distance to relax to a distance of 2.71(5) Å (not shown). The partially occupied Co5 position is also split into an octahedral coordination of six positions with a Co5—Sn9 bond distance of 4 × 2.56(2) Å. The splitting of the Co5 and Sn9 positions has been previously found for Sm$_{117}$Co$_{52}$Sn$_{112}$;[21] however, it was not necessary to split the split Co7 position for the Gd analogue. It is worth noting that all atoms are shown in our structural depiction except the Gd5 and Gd6 (split position) atoms (not shown for clarity) which are located about the edges and faces of the Sn9 cages, respectively.

The Co5—Sn9 and Co3—Sn1 bond distances of 2.536(2) and 2.560(2) Å, respectively, are less than the sum of the covalent radii of Co (1.26 Å) and Sn (1.41 Å). The bond distances are also far greater than the sum of the largest ionic radii given by Shannon for both Sn and Co.[25] Therefore, the

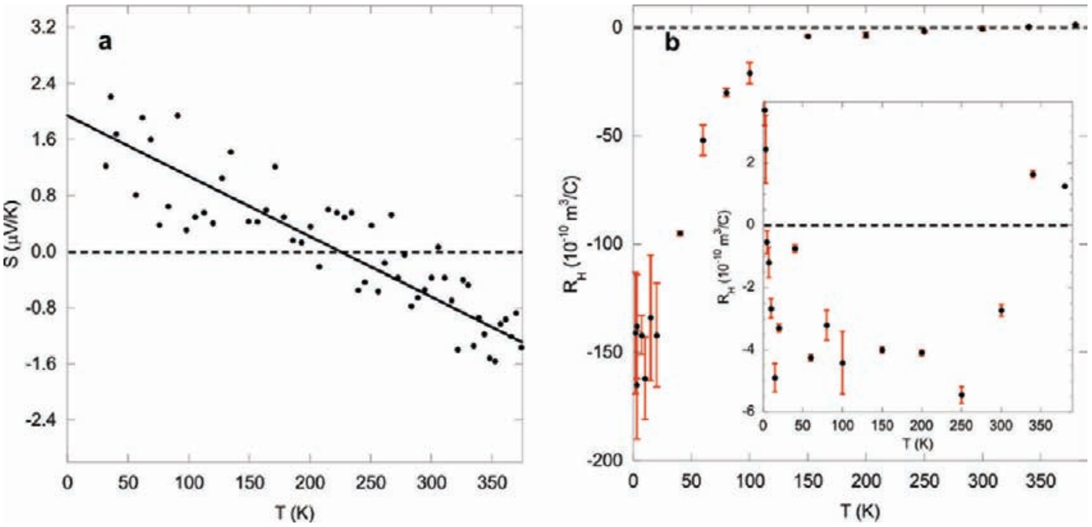

Figure 5. (a) Thermopower as a function of temperature for $Gd_{117}Co_{56}Sn_{112}$ from 30 to 375 K. The solid line is a linear best-fit for all data points, and the dashed line indicates the zero line of the thermopower. (b) Low-field and high-field (inset) Hall coefficient as a function of temperature for $Gd_{117}Co_{56}Sn_{112}$. The dashed lines indicate the zero line of the Hall coefficient.

Co−Sn bonds appear to have a covalent-ionic character, similar to the Rh−Sn bonds reported for the $Ln_3Rh_4Sn_{13}$ and $Er_5Rh_6Sn_{18}$ compounds.[28,33,34]

Physical Properties. The temperature dependence of the electrical resistivity of single crystal $Gd_{117}Co_{56}Sn_{112}$ from 2 to 375 K is shown in Figure 4a. The resistivity increases with decreasing temperature ($d\rho/dT < 0$) throughout the entire temperature range, with the lowest measured value of 0.510 mΩ•cm at the highest measured temperature of 375 K. A small kink in the resistivity at low temperature near 3.5 K is due to a small amount of Sn inclusion (residual flux) in the crystal, which is suppressed by the application of a magnetic field (Supporting Information, Figure S1, inset). (The superconducting transition temperature of Sn is $T_{c\text{-}Sn} = 3.7$ K.) The negative slope in the low-temperature region (3−50 K) indicates the transport is dominated by thermal activation, where the carrier density varies as $e^{-E_g/2k_BT}$. Thus, the slope of $\ln(\rho)$ vs $1/(2k_BT)$ gives a good approximation of the energy gap, E_g. Using this approximation, we find $E_g \sim 0.004$ eV or ∼50 K. The very small value for E_g suggests a pseudogap, as opposed to a real energy gap, exists in the density of states at the Fermi level. Similar resistivity trends have been noted in quasicrystalline systems,[35,36] which have been explained by a pseudogap, and in amorphous transition metal alloys.[37] $Gd_{117}Co_{56}Sn_{112}$ exhibits negative magnetoresistance, shown in Supporting Information, Figure S1, with maximum values at 14 T of ∼ −14%, −12%, and −3% at 3, 20, and 70 K, respectively.

Figure 4b shows the electronic (κ_e), lattice (κ_L), and total (κ_T) thermal conductivity data for $Gd_{117}Co_{56}Sn_{112}$ from 2 to 375 K. κ_e was estimated using the resistivity data in conjunction with $\kappa_e = L_0T/\rho$, and κ_L was calculated using the relationship $\kappa_L = \kappa_T + \kappa_e$. The total thermal conductivity of $Gd_{117}Co_{56}Sn_{112}$ is small over the entire measured temperature range and comparable to Al-based icosahedral quasicrystals.[35] The calculated room temperature value for κ_L is exceptionally low at 0.28 W/(m·K). A comparison can be made to thermoelectric materials, which typically have low κ_L values. The κ_L of $Gd_{117}Co_{56}Sn_{112}$ is lower than all the best known thermoelectric materials, including $Yb_{14}MnSb_{11}$, which has an estimated room temperature lattice thermal conductivity of ∼0.55 W/(m•K).[38] κ_L has a maximum value of ∼0.50 W/(m•K) at 67 K, which is $\sim\Theta_D/5$ (vide infra)—the relationship which typically relates Θ_D to the maximum thermal conductivity in metallic systems.[4] Other solid materials have lower thermal conductivities, such as bulk silica aerogel[39,40] and WSe_2;[41] however, the former is a porous, two-phase insulator, and the latter consists of disordered two-dimensional thin films. (As a comparison, the thermal conductivity of bulk single-crystalline WSe_2 is ∼1.5 W/(m•K) near room temperature.)[41] In this regard, the lattice thermal conductivity of $Gd_{117}Co_{56}Sn_{112}$ is extremely low for a bulk single crystal.

The low lattice thermal conductivity in $Gd_{117}Co_{56}Sn_{112}$ can be explained by the large number of atoms (N) in the primitive unit cell, its complex structural units, the high atomic masses of its constituent elements, and its large unit cell volume. Phonon scattering processes can be classified as two types N and U, where N-processes (normal) conserve phonon momentum during the collision process, and U-processes (umklapp) do not.[4] Thus, umklapp scattering is the dominant mechanism at reducing the thermal conductivity in crystalline solids (at high temperatures). After a U-process, the resulting phonon momentum wave vector lies outside the Brillouin zone. The wave vector, however, is equivalent to the one in the same zone via a transformation with a reciprocal lattice vector. The large lattice constants of $Gd_{117}Co_{56}Sn_{112}$ give rise to a small Brillouin zone (in momentum or reciprocal space). Thus, for a given phonon momentum, the likelihood of U-processes increases.

Unlike other complex unit cell materials with low thermal conductivity,[42] the low electrical resistivity of $Gd_{117}Co_{56}Sn_{112}$ results in the total thermal conductivity being dominated by the electronic contribution. In addition, an increase in the slope of the lattice thermal conductivity is observed at high temperatures above 300 K which is unusual, as the lattice thermal conductivity in most bulk solids tends to decrease with increasing temperature. A large enhancement of κ_e relative to κ_L at higher temperature (>100 K) can occur in small band gap semiconductors and semimetals[4] and is indicative of bipolar diffusion effects (conduction of electrons and holes), an interpretation also supported by the thermopower and Hall coefficient data presented below. This behavior in the thermal conductivity is consistent with the presence of a symmetric pseudogap at the Fermi level. Such a description was used to model the thermal conductivity in structurally complex Al alloys.[42]

Table 3. Estimated Lattice Thermal Conductivity (κ_L), Electrical Resistivity (ρ), and $1/(\rho\kappa_L)$ Values at 300 K of Some of the Best Known Bulk Thermoelectric Materials

material	κ_L (W/(m·K))	ρ (10^{-5} Ω·m)	$1/(\rho\kappa_L)$ (10^3 K/(Ω·W))
$(Bi/Sb)_2Te_3$[44 a]	0.6	0.794	209.9
$(Bi/Sb)_2Te_3$[44 b]	0.9	1	111.1
$Si_{0.75}Ge_{0.25}$[45]	3.5	1.1	26.0
$Ba_{0.08}La_{0.05}Yb_{0.04}Co_4Sb_{12}$[46 c]	1.16	0.417	206.7
$PbTe_{0.5}Se_{0.5}$[47]	0.58	2	86.2
TAGS-75[8]	0.8	1.6	78.1
$MnSi_{1.75}$[48,49]	2.9	1.4	24.6
$Yb_{14}MnSb_{11}$[38]	0.55	2	90.9
Ag_9TlTe_5[50]	0.23	130	3.3
$Gd_{117}Co_{56}Sn_{112}$	0.28	0.52	686.8

[a] Nanocrystalline sample. [b] Zone-melted sample. [c] Skutterudite structure.

Figure 5a shows the Seebeck coefficient as a function of temperature from 30 to 375 K. The largest value recorded for the Seebeck coefficient is 2.2 μV/K, which corresponds to the lowest measured temperature. The thermopower has a negative temperature coefficient and crosses zero at ~225 K. Hall resistivity (ρ_H) as a function of magnetic field shows an anomalous Hall coefficient (R_H) behavior (Supporting Information, Figure S2); thus, the R_H data were fit at low and high field. R_H as a function of temperature is shown in Figure 5b. Typically, the sign of R_H mirrors that of the Seebeck coefficient, signifying the dominant charge carrier as electrons (negative) or holes (positive); however, R_H for $Gd_{117}Co_{56}Sn_{112}$ shows the opposite trend. R_H is negative at low temperatures, and reduces in magnitude as a function of temperature which is opposite to the thermopower behavior. The Hall coefficient approaches zero at ~300 K (Figure 5b), slightly higher in temperature than the zero crossing of the thermopower ~225 K. The zero crossing in the Hall coefficient and thermopower, as well as their low values, indicate that $Gd_{117}Co_{56}Sn_{112}$ is a partially compensated (bipolar) material throughout the entire measured temperature range.

In a bipolar material, the full form of the electronic thermal conductivity is represented by $\kappa_e = \kappa_{e,1} + \kappa_{e,2} + [(\sigma_1\sigma_2)/(\sigma_1 + \sigma_2)](S_1 - S_2)^2T$, where the numbers 1 and 2 denote the types of charge carriers, σ is electrical conductivity, and S is the Seebeck coefficient. Typically, the third term is ignored in κ_e calculations; however, the value becomes significant in bipolar materials, when S_1 and S_2 are opposite in sign and σ_1 and σ_2 are of equal magnitude. Since $Gd_{117}Co_{56}Sn_{112}$ appears to be a bipolar material, the calculated value of κ_e should be considered as a lower limit, or more importantly, our calculated value of κ_L represents its maximum value.

Further insight into how well $Gd_{117}Co_{56}Sn_{112}$ approximates a PGEC is gained by calculating the value $1/(\rho\kappa_L)$, where the limit of $1/(\rho\kappa_L) \to \infty$ represents the ideal case. Table 3 shows the room temperature values of $1/(\rho\kappa_L)$ for $Gd_{117}Co_{56}Sn_{112}$ and some of the best-known thermoelectrics. As shown in the Table 3, single-crystalline $Gd_{117}Co_{56}Sn_{112}$ has a value of $1/(\rho\kappa_L) = 6.87 \times 10^5$ K/(Ω·W). This value is well above those for any of the conventional thermoelectric materials, including a factor of 6 better than Bi_2Te_3.

Figure 6a shows zero-field-cooled (ZFC) and field-cooled (FC) magnetic susceptibility data for $Gd_{117}Co_{49}Sn_{116}$ from 3 to 290 K measured at 0.1 T. The ZFC data are fit using the modified Curie–Weiss law $\chi = \chi_0 + C/(T - \theta_{CW})$, where χ_0 is the temperature-independent susceptibility, C is the Curie–Weiss constant, and θ_{CW} is the Curie–Weiss temperature. Our fit in the temperature range 150–292 K gives χ_0 = 0.0066(4) emu/(mol·Gd), θ_{CW} = 16(2) K, and C = 7.89(15) emu/(mol·Gd). The experimentally calculated magnetic moment of μ_{eff} = 7.94(7) μ_B/Gd is in excellent agreement with the theoretical magnetic moment of μ_{calc} = 7.94 μ_B/Gd. The ZFC and FC susceptibility data show an apparent antiferromagnetic transition at 13 K, which is similar in magnitude to the fitted θ_{CW} = 16(2) K, but the positive θ_{CW} sign and negative magnetoresistance suggest ferromagnetic interactions. The presence of ferromagnetic interactions is reinforced by a

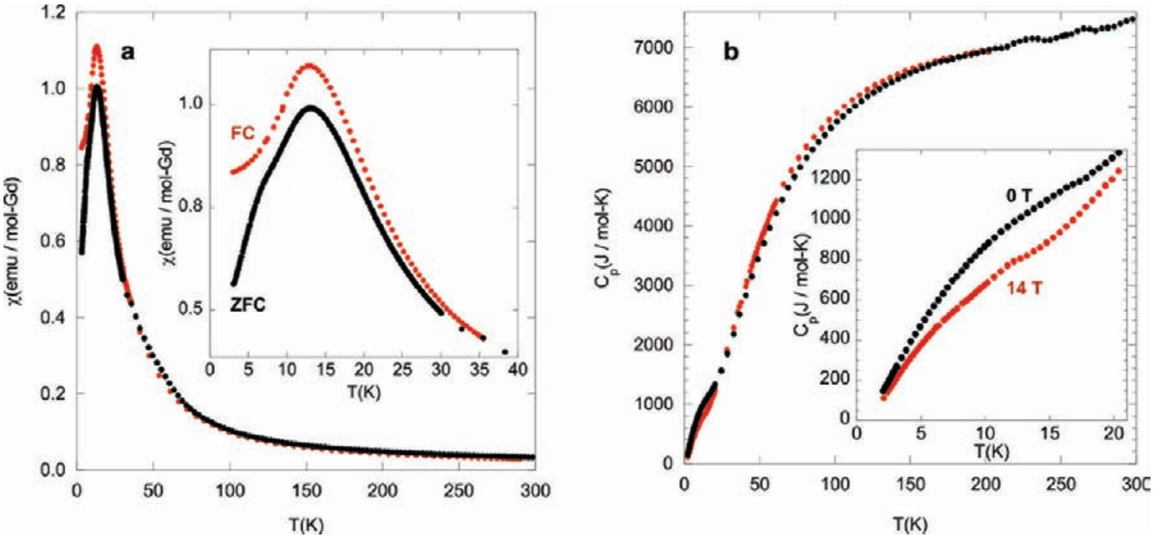

Figure 6. (a) Magnetic susceptibility as a function of temperature for $Gd_{117}Co_{56}Sn_{112}$ from 3 to 300 K under ZFC (black circles) and FC (red circles) conditions at 0.1 T. (b) Heat capacity (C_p) as a function of temperature for $Gd_{117}Co_{56}Sn_{112}$ from 2 to 300 K at 0 T (black circles) and 14 T (red circles). The inset shows C_p vs T from 2 to 21 K at 0 and 14 T.

divergence in the ZFC and FC magnetic susceptibility shown in Figure 6a, inset. This behavior is similar to the previously reported Tb (θ_{CW} = 59 K) and Dy (θ_{CW} = 18 K) analogues[21] which also exhibit antiferromagnetic transitions at 22 and 11 K, respectively. Field-dependent magnetization taken at 3 and 12 K (Supporting Information, Figure S3) shows a nonlinear dependence of magnetization as a function of field and shows no sign of saturation at high field; however, the measurement taken at 3 K shows a small hysteresis at low field, which is not present in the 12 K measurement.

Figure 6b shows the temperature dependence of the heat capacity at 0 and 14 T. At low temperatures, there are anomalies at ~18 and ~14 K for the 0 and 14 T data, respectively. These anomalies (Figure 6b, inset), which appear to be suppressed to a lower temperature with the application of a magnetic field, support our observation of an antiferromagnetic transition ~13 K from the magnetic susceptibility data. Prior to the magnetic phase transition, we find that specific heat shows linear behavior from 16 to 33 K at 14 T when plotted as C_p/T vs T^2 (Supporting Information, Figure S4). Thus, we fit data using $C_p/T = \gamma + \beta T^2$, where γ and β are the electronic and phonon contributions to the heat capacity, respectively. The fit gives γ = 55.17(9) J/(mol(F.U.)·K^2) and a Debye temperature Θ_D = 336.3(12) K using the relationship $\beta = 12\pi^4 RN/5\Theta_D{}^3$, where R = 8.314 J/(mol·K) and N is the number of atoms per formula unit. A Debye temperature >300 K is expected since the heat capacity does not saturate up to the maximum measured temperature of 300 K. An additional anomaly at ~6 K can be seen in the C_P/T vs T^2 plot, which is likely an additional magnetic transition. This transition corresponds to the shoulder at 6 K in the ZFC susceptibility shown in Figure 6a, inset.

We began our study of $Gd_{117}Co_{56}Sn_{112}$ with the assumption that the lattice thermal conductivity should be exceptionally low due to the complexity of the crystal structure. The results exceeded our expectation with a lattice thermal conductivity of κ_L = 0.28 W/(m·K) at 300 K, which represents one of the lowest values ever measured for a bulk crystalline material. To our surprise, $Gd_{117}Co_{56}Sn_{112}$ also has a low electrical resistivity with semiconducting-like behavior, which gives a $1/(\rho\kappa_L)$ value of 6.87 × 10^5 K/(Ω·W). The low Seebeck coefficient precludes $Gd_{117}Co_{56}Sn_{112}$ from joining the list of viable thermoelectric materials in its pure form; however, doping studies and high-temperature transport measurements on $Gd_{117}Co_{56}Sn_{112}$ may prove effective at improving its performance. Tuning the Fermi level by chemically doping through a pseudogap in similar materials, such as Si-doped Al−Re alloys,[43] has produced significant enhancements in thermopower. Furthermore, we are compelled to investigate $Gd_{117}Co_{56}Sn_{112}$ as a potential *thermomagnetic* material. A simple explanation for a zero Hall coefficient is to assume equal numbers of electrons and holes with equal mobilities. Of course, the real material is undoubtedly more complex. Nonetheless, thermomagnetic cooling relies on contributions from both types of charge carriers, which are clearly intrinsic to this material. Another potential application is a device that requires electrical conduction but a high degree of thermal shielding, where very few materials meet these criteria. In any case, the extremely low lattice thermal conductivity and large value of $1/(\rho\kappa_L)$ establishes $Gd_{117}Co_{56}Sn_{112}$ as a new class of materials deserving of further exploration.

■ ASSOCIATED CONTENT

Ⓢ Supporting Information

Resistivity, Hall resistivity, magnetization as a function of magnetic field, and heat capacity divided by temperature (C_p/T) as a function of temperature squared (T^2) for $Gd_{117}Co_{56}Sn_{112}$. This material is available free of charge via the Internet at http://pubs.acs.org.

■ AUTHOR INFORMATION

Corresponding Author

E-mail: jchan@lsu.edu. Tel.: (225) 578-2695. Fax: (225) 578-3458

Notes

The authors declare no competing financial interest.

■ ACKNOWLEDGMENTS

J.Y.C. acknowledges Louisiana Board of Regents and NSF DMR 1063735. D.P.Y. acknowledges NSF DMR 1005764 for funding. R.J. acknowledges NSF DMR 1002622 for funding. D.C.S. acknowledges Brenton Drake, Melissa Menard, William Phelan, and Frank Fronczek for useful discussion.

■ REFERENCES

(1) Mahan, G. D. *Good Thermoelectrics*; Academic Press Inc: San Diego, CA, 1998; Vol. *51*, pp 81−157.
(2) Snyder, G. J.; Toberer, E. S. *Nat. Mater.* **2008**, *7*, 105−114.
(3) Tritt, T. M. *Annu. Rev. Mater. Res.* **2011**, *41*, 433−448.
(4) Tritt, T. M. *Thermal Conductivity Theory, Properties and Applications*; Kluwer Academic: New York, 2004; p 290.
(5) Toberer, E. S.; May, A. F.; Snyder, G. J. *Chem. Mater.* **2010**, *22*, 624−634.
(6) Slack, G. A. New Materials and Performance Limits for Thermoelectric Cooling. In *CRC Handbook of Thermoelectrics*; Rowe, D. M., Ed.; CRC Press: Boca Raton, FL, 1995; pp 407−440.
(7) Snyder, G. J.; Christensen, M.; Nishibori, E.; Caillat, T.; Iversen, B. B. *Nat. Mater.* **2004**, *3*, 458−463.
(8) Yang, S. H.; Zhu, T. J.; Sun, T.; Zhang, S. N.; Zhao, X. B.; He, J. *Nanotechnology* **2008**, *19*.
(9) Hsu, K. F.; Loo, S.; Guo, F.; Chen, W.; Dyck, J. S.; Uher, C.; Hogan, T.; Polychroniadis, E. K.; Kanatzidis, M. G. *Science* **2004**, *303*, 818−821.
(10) DiSalvo, F. J. *Science* **1999**, *285*, 703−706.
(11) Bodak, O. P.; Gladyshe, Ei *Sov. Phys. Crystallogr.* **1970**, *14*, 859−.
(12) Yan, J. L.; Xu, Y.; Long, Q. X.; Zhu, J. M.; Zhuang, Y. H. Springer: New York, 2009; pp 435−442.
(13) Otwinowski, Z.; Minor, W. *Methods Enzymol.* **1997**, *276*, 307−326.
(14) Burla, M. C.; Carrozzini, B.; Cascarano, G. L.; Giacovazzo, C.; Polidori, G. *Z. Kristallogr.* **2002**, *217*, 629−635.
(15) Sheldrick, G. M. *Acta Crystallogr.* **2008**, *64*, 112−122.
(16) Salamakha, P.; Sologub, O.; Bocelli, G.; Otani, S.; Takabatake, T. *J. Alloys Compd.* **2001**, *314*, 177−180.
(17) Pecharsky, V. K.; Bodak, O. I.; Belsky, V. K.; Starodub, P. K.; Mokra, I. R.; Gladyshevskii, E. I. *Kristallografiya* **1987**, *32*, 334−338.
(18) Morozkin, A. V.; Seropegin, Y. D.; Portnoy, V. K.; Sviridov, I. A.; Leonov, A. V. *Mater. Res. Bull.* **1998**, *33*, 903−908.
(19) Cirafici, S.; Canepa, F.; Manfrinetti, P.; Napoletano, M. *J. Alloys Compd.* **2001**, *317*−*318*, 550−555.
(20) He, W.; Zhang, J. L.; Yan, J. L.; Fu, Y. C.; Zeng, L. M. *J. Alloys Compd.* **2010**, *491*, 49−52.
(21) Kovnir, K.; Shatruk, M. *Eur. J. Inorg. Chem.* **2011**.
(22) Salamakha, P.; Demchenko, P.; StepienDamm, J. *J. Alloys Compd.* **1997**, *260*, L1−L3.
(23) Hohnke, D.; Parthé, E. *Acta Crystallogr.* **1966**, *21*, 435−437.

(24) Ganguli, A. K.; Guloy, A. M.; Leonescamilla, E. A.; Corbett, J. D. *Inorg. Chem.* **1993**, *32*, 4349−4353.
(25) Shannon, R. D. *Acta Crystallogr.* **1976**, *32*, 751−767.
(26) Hlukhyy, V.; Eck, S.; Fässler, T. F. *Inorg. Chem.* **2006**, *45*, 7408−7416.
(27) Lei, X. W.; Zhong, G. H.; Li, M. J.; Mao, J. G. *J. Solid State Chem.* **2008**, *181*, 2448−2455.
(28) Hodeau, J. L.; Chenavas, J.; Marezio, M.; Remeika, J. P. *Solid State Commun.* **1980**, *36*, 839−845.
(29) Pires, M. A.; Ferreira, L. M.; Duque, J. G. S.; Urbano, R. R.; Aguero, O.; Torriani, I.; Rettori, C.; Bittar, E. M.; Pagliuso, P. G. *J. Appl. Phys.* **2006**, *99*, 1−3.
(30) Pani, M.; Manfrinetti, P.; Palenzona, A.; Dhar, S. K.; Singh, S. *J. Alloys Compd.* **2000**, *299*, 39−44.
(31) Zhong, G. H.; Lei, X. W.; Mao, J. G. *Phys. Rev. B* **2009**, *79*, 1−13.
(32) Hoffmann, S.; Fassler, T. F. *Inorg. Chem.* **2003**, *42*, 8748−8754.
(33) Miraglia, S.; Hodeau, J. L.; Marezio, M.; Laviron, C.; Ghedira, M.; Espinosa, G. P. *J. Solid State Chem.* **1986**, *63*, 358−368.
(34) Hodeau, J. L.; Marezio, M.; Remeika, J. P. *Acta Crystallogr.* **1984**, *40*, 26−38.
(35) Gianno, K.; Sologubenko, A. V.; Chernikov, M. A.; Ott, H. R.; Fisher, I. R.; Canfield, P. C. *Mater. Sci. Eng.—Struct. Mater. Prop. Microstruct. Process.* **2000**, *294*, 715−718.
(36) Takeuchi, T.; Onogi, T.; Otagiri, T.; Mizutani, U.; Sato, H.; Kato, K.; Kamiyama, T. *Phys. Rev. B* **2003**, 68.
(37) Rapp, O.; Jackle, J.; Frobose, K. *J. Phys. F Met. Phys.* **1981**, *11*, 2359−2366.
(38) Cox, C. A.; Toberer, E. S.; Levchenko, A. A.; Brown, S. R.; Snyder, G. J.; Navrotsky, A.; Kauzlarich, S. M. *Chem. Mater.* **2009**, *21*, 1354−1360.
(39) Richter, K.; Norris, P. M.; Tien, C.-L. Aerogels: applications, structure and heat transfer phenomena. In *Annual Review of Heat Transfer*; Tien, C.-L., Ed.; Begell House, Inc.: New York, 1995; Vol. *VI*, pp 61−114.
(40) Norris, P. M.; Shrinivasan, S. Aerogels: unique material, fascinating properties, and unlimited applications. In *Annual Review of Heat Transfer*; Prasad, B., Jaluria, Y., Chen, G., Eds.; Begell House, Inc.: New York, 2005; Vol. *XIV*, pp 385−408.
(41) Chiritescu, C.; Cahill, D. G.; Nguyen, N.; Johnson, D.; Bodapati, A.; Keblinski, P.; Zschack, P. *Science* **2007**, *315*, 351−353.
(42) Takeuchi, T. *J. Electron. Mater.* **2009**, *38*, 1354−1359.
(43) Takeuchi, T.; Otagiri, T.; Sakagami, H.; Kondo, T.; Mizutani, U.; Sato, H. *Phys. Rev. B* **2004**, *70*.
(44) Poudel, B.; Hao, Q.; Ma, Y.; Lan, Y. C.; Minnich, A.; Yu, B.; Yan, X. A.; Wang, D. Z.; Muto, A.; Vashaee, D.; Chen, X. Y.; Liu, J. M.; Dresselhaus, M. S.; Chen, G.; Ren, Z. F. *Science* **2008**, *320*, 634−638.
(45) Meddins, H. R.; Parrott, J. E. *J. Phys. C Solid State* **1976**, *9*, 1263−1276.
(46) Shi, X.; Yang, J.; Salvador, J. R.; Chi, M. F.; Cho, J. Y.; Wang, H.; Bai, S. Q.; Yang, J. H.; Zhang, W. Q.; Chen, L. D. *J. Am. Chem. Soc.* **2011**, *133*, 7837−7846.
(47) Li, J. Q.; Li, S. P.; Wang, Q. B.; Wang, L.; Liu, F. S.; Ao, W. Q. *J. Alloys Compd.* **2011**, *509*, 4516−4519.
(48) Vining, C. B., Thermoelectric properties of silicides. In *CRC Handbook of Thermoelectrics*; Rowe, D. M., Ed. CRC Press: Boca Raton, FL, 1995; pp 277−298.
(49) Zaitsev, V. K. Thermoelectric properties of anisotropic $MnSi_{1.75}$. In *CRC Handbook of Thermoelectrics*; Rowe, D. M., Ed.; CRC Press: Boca Raton, FL, 1995; pp 299−309.
(50) Kurosaki, K.; Kosuga, A.; Muta, H.; Uno, M.; Yamanaka, S. *Appl. Phys. Lett.* **2005**, *87*, 061919-1−061919-3.